



# Wall drag modification by large deformable droplets in turbulent channel flow



Luca Scarbolo\*, Alfredo Soldati

<sup>a</sup> Department of Elec. Manag. and Mechanical Engineering, University of Udine, 33100 Udine, Italy

<sup>b</sup> Department of Fluid Mechanics, CISM, 33100 Udine, Italy

## ARTICLE INFO

### Article history:

Received 23 December 2013

Accepted 25 June 2014

Available online 3 July 2014

### Keywords:

Turbulence

Droplets

Drag

Phase field model

Cahn–Hilliard

## ABSTRACT

The role of deformability in the wall-drag modification produced by the dispersion of large deformable droplets in turbulence is investigated by Direct Numerical Simulations (DNS) of a turbulent channel flow ( $Re_\tau = 150$ ) coupled with the Phase Field Model (PFM) description of the droplets. The two fluids have the same density and viscosity, and a wide range of interface deformability is considered by changing the Weber number:  $We = 0.18$ – $2.8$ . The results show wall-drag modifications that depend on the droplets deformability: when the deformability is low (small  $We$ ), a significant Drag Enhancement (DE) is observed; increasing the deformability the DE is reduced and negligible effects are observed when the Weber number is sufficiently large. The DE is likely due to droplets velocity that reduces increasing the deformability, introducing an obstruction to the flow and increasing drag.

© 2014 Elsevier Ltd. All rights reserved.

## 1. Introduction

Swarms of large deformable bubbles dispersed in wall bounded turbulence produce significant modifications of the wall drag; these effects have been investigated by many authors, focusing on the quantification of drag and evidencing situations where large amount of Drag Reduction (DR) can be observed [1–3]. In spite of its practical relevance, the mechanism underpinning the wall-drag modification in presence of large deformable bubbles is still not clear and only few recent studies proposed a detailed analyses of the droplet–turbulence interactions [4,5]. The Direct Numerical Simulations (DNS) of Lu et al. [4] highlighted the role of bubbles deformability in the wall-drag modification produced by a large number of bubbles with the same viscosity of the surrounding fluid and with a small density ratio ( $\rho_f/\rho_d = 10$ ). They observed that deformable bubbles released in a turbulent channel flow could produce Drag Reduction (DR) or Drag Enhancement (DE), according to their deformability. Two mechanisms were proposed: (i) bubbles characterized by large deformability produced a near-wall streamwise vorticity canceling, resulting in DR; (ii) bubbles with small deformability were slowed down by the near-wall flow field, producing an obstruction to the flow and resulting to DE. The recent experimental work of van Gils et al. [5] showed important

DR (up to 40%) when large deformable bubbles (with viscosity ratio  $\rho_f\nu_f/\rho_b\nu_b = 100$  and a density ratio  $\rho_f/\rho_d = 1000$ ) were released in a turbulent Taylor–Couette flow, emphasizing the central role of the bubbles deformability. In order to further clarify the role of the deformability in the context of large deformable bodies dispersed in turbulent wall-bounded flows, in this work the problem has been simplified neglecting the density and the viscosity differences between the two fluids, retaining the surface tension  $\sigma$  only. The physical system defined through these simplifications is governed by two leading effects: (i) droplet deformability, that is controlled by the surface tension; (ii) droplet inertia that is comparable to that of the surrounding fluid. As a result the problem is set to its simplest configuration, highlighting the surface tension effects and allowing a parametric analysis of the droplet deformability that can be varied between two limit cases: the single phase flow ( $\sigma = 0$ ,  $We \rightarrow \infty$ ) and the dispersion of rigid fluid spheres ( $\sigma \rightarrow \infty$ ,  $We = 0$ ). To the best of our knowledge this work represents one of the first attempts to analyze and model the interaction between turbulence and deformable droplets, considering only the surface tension effects.

## 2. Governing equations

In this work the wall-drag modification produced by a large number of deformable droplets dispersed in wall-bounded turbulence has been studied. The flow field evolution has been described with DNSs of a modified incompressible Navier–Stokes equations

\* Corresponding author. Tel.: +39 0432855005.

E-mail addresses: [luca.scarbolo@uniud.it](mailto:luca.scarbolo@uniud.it) (L. Scarbolo), [soldati@uniud.it](mailto:soldati@uniud.it) (A. Soldati).

coupled with the Phase Field Model (PFM) description of the fluid–fluid interfaces.

### 2.1. The phase field model

In the PFM, the interface between two fluids is considered as a layer of finite thickness rather than a sharp discontinuity. Across the interfacial layer the physical properties of the fluid components vary in a smooth and continuous way from one fluid to the other. The state of the system is described, at any time, by a scalar order parameter  $\phi$ , which is a function of the position vector  $\mathbf{x}$ . The order parameter directly represents one of the physical properties of the fluid, such as its density, its molar concentration, etc.; all the remaining properties are in turn modeled as proportional to the scalar order parameter  $\phi(\mathbf{x})$  [6,7]. Due to the continuous description of the interface, also the order parameter is continuous over the entire domain and it shows smooth variations across the interface between single fluid regions, where it assumes mostly uniform values. Coupling the continuous representation of the two fluid field with a transport equation of the order parameter, the system evolution can be resolved in time. One of the best-known PFM is the Cahn–Hilliard equation [8,9], where the evolution of the order parameter is driven by the minimization of a thermodynamical conservative chemical potential. As a result the conservation of the phase field is ensured and the diffusion of the interfacial layer is overcome, granting more accuracy in the computation of the interfacial forces [7] and avoiding the major drawback of the most common interface-tracking methods [10]. The convective Cahn–Hilliard equation is written as follows:

$$\frac{\partial \phi}{\partial t} = -\mathbf{u} \cdot \nabla \phi + M \nabla^2 \mu, \quad (1)$$

where  $\mathbf{u}$  is the velocity field,  $M$  is the mobility parameter that controls the interface relaxation time and  $\mu$  is a chemical potential that controls the interfacial layer behavior. Eq. (1) models the evolution in time of a diffuse interface, in particular it can describe the conservative advection of a diffuse interface [11,12] and complex changes in the interface topology. The chemical potential  $\mu$  is defined in terms of the free energy functional  $f[\phi]$  as follows:

$$\mu = \frac{\delta f[\phi(\mathbf{x})]}{\delta \phi}, \quad (2)$$

where  $f[\phi]$  is a conservative, thermodynamically consistent functional that can assume suitable definitions according to the problem under analysis and it. The PFM representation of an immiscible binary mixture of isothermal fluids is given by the following free energy functional:

$$\begin{aligned} f[\phi(\mathbf{x})] &= f_{id} + \frac{1}{2} \kappa |\nabla \phi|^2 \\ &= \frac{\alpha}{4} \left( \phi - \sqrt{\frac{\beta}{\alpha}} \right)^2 \left( \phi + \sqrt{\frac{\beta}{\alpha}} \right)^2 + \frac{1}{2} \kappa |\nabla \phi|^2. \end{aligned} \quad (3)$$

In this work, the scalar order parameter  $\phi$  represents the relative concentration of the two fluid components. The first term on the right-hand-side of Eq. (3),  $f_{id}$ , is the ideal part of the free energy that accounts for the tendency of the system to separate into pure fluid clusters. For two immiscible fluids, the phobic behavior is described by a double-well formulation which shows two minima corresponding to the two stable fluid phases that are defined through the positive constants  $\alpha$  and  $\beta$ . The two fluids are allowed to mix into the interfacial layer where they store a mixing energy which is accounted by the non-local term  $1/2\kappa|\nabla\phi|^2$  of Eq. (3) and which is the source of the surface tension in the PFM. The relative concentration equilibrium profile across the interface is given by

the competition of the two terms appearing in the free energy formulation and can be obtained by minimizing the free energy functional with respect to the variations of the order parameter:

$$\mu = \frac{\delta f[\phi]}{\delta \phi} = 0 \Rightarrow \alpha \phi^3 - \beta \phi - \kappa \nabla^2 \phi = 0. \quad (4)$$

Integration of Eq. (4) for a one-dimensional planar interface, where  $\phi(z \rightarrow \pm\infty) = \phi_{\pm}$ , yields two stable solutions  $\phi_{\pm} = \pm\sqrt{\beta/\alpha}$  and the following non-uniform solution:

$$\phi(z) = \phi_+ \tanh\left(\frac{z}{\sqrt{2}\xi}\right). \quad (5)$$

The capillary width  $\xi = \sqrt{\kappa/\beta}$  is the interface length scale;  $0.9\phi_- \leq \phi \leq 0.9\phi_+$  in a layer of  $4.164\xi$  that contains the 98.5% of the interface surface tension [6,12]. At the equilibrium, the surface tension  $\sigma$  is:

$$\sigma = \kappa \int_{-\infty}^{+\infty} \left(\frac{d\phi}{dz}\right)^2 dz = \frac{\sqrt{8}}{3} \frac{\kappa^{\frac{1}{2}} \beta^{\frac{3}{2}}}{\alpha}. \quad (6)$$

Once the interface thickness  $\xi$  and the equilibrium solutions  $\phi_{\pm}$  are chosen, Eq. (6) allows to define the free energy parameters  $\alpha$ ,  $\beta$  and  $\kappa$  necessary to achieve the desired surface tension value. The derivation described above has been adopted and reviewed by several authors [13,14] and the convergence of Eq. (1) to the “sharp interface limit” has been recently proven [15]. In particular, although the fictitious widening of the interface necessary for its numerical resolution,<sup>1</sup> the PFM can describe the desired value of  $\sigma$  by defining the free energy functional coefficients and adopting a proper scaling between the capillary width  $\xi$  and the interface mobility  $M$  [12,15].

### 2.2. Coupling with the flow field

The evolution of the velocity field  $\mathbf{u}$  is described by the incompressible Navier–Stokes equations provided by a phase field-dependent surface force [16]:

$$\nabla \cdot \mathbf{u} = 0, \quad (7)$$

$$\frac{\partial \mathbf{u}}{\partial t} = -\mathbf{u} \cdot \nabla \mathbf{u} - \nabla p + \nu \nabla^2 \mathbf{u} + \mu \nabla \phi, \quad (8)$$

where  $p$  is the pressure term and  $\nu$  is the kinematic viscosity. The coupled Chan–Hilliard/Navier–Stokes (CHNS) Eqs. 1, 7 and 8 is the so-called “Model-H” [17], where the surface tension forcing  $\mu \nabla \phi$  is derived from the Korteweg stress.

## 3. Numerical simulations

### 3.1. Geometry and numerical scheme

In this work a swarm of droplets of initial diameter  $d$  dispersed in a fully developed turbulent channel flow is simulated; the two fluids are considered immiscible, incompressible, Newtonian, density-matched and viscosity-matched. With this assumptions the system is set to its simplest configuration, allowing to isolate the surface tension effects and the role of droplets deformability on the wall-drag modification. With reference to Fig. 1 the coordinate system is located at the center of the channel and  $x$ -,  $y$ - and  $z$ -axes point in the streamwise, spanwise and wall-normal directions, respectively. The size of the channel is  $4\pi h \times 2\pi h \times 2h$  in  $x$ ,  $y$ , and  $z$  directions, respectively, and  $h$  is the channel half-height. The droplets are initialized by superposing the phase field  $\phi$  over

<sup>1</sup> At least three mesh-points are necessary to fully resolve the interface with the current methodology employed. Larger number of mesh-points can be required according to the accuracy of the numerical scheme adopted.

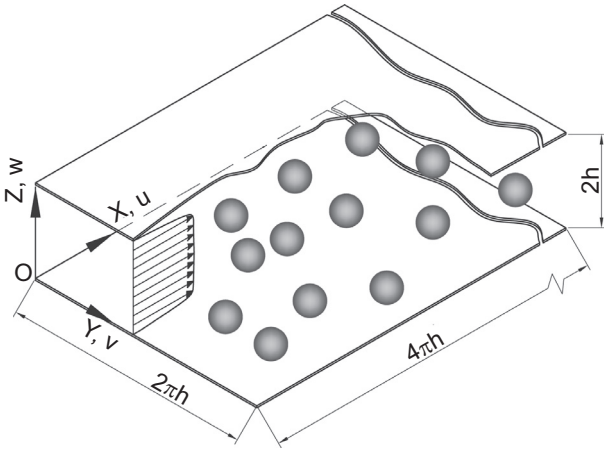


**Fig. 1.** Schematics of the problem under analysis: dispersion of a swarm of large deformable droplets in a turbulent channel flow.

a fully developed turbulent flow obtained from previous single phase DNSs in a statistically steady state. The CHNS Eqs. 1, 7 and 8 have been rewritten in a non-dimensional form, where the superscript “-” indicates non-dimensional quantities. The scaling variables here adopted are  $U_\tau$ ,  $h$ , and  $\phi_+$ , where  $U_\tau = \sqrt{\tau_w/\rho}$  is the shear velocity based on the wall shear stress  $\tau_w$  and the fluid density  $\rho$ ;  $\phi_+ = \sqrt{\beta/\alpha}$  is one of the two stable solutions given by the chemical potential (2).

$$\frac{\partial \phi^-}{\partial t^-} = -\mathbf{u}^- \cdot \nabla \phi^- + \frac{1}{Pe} \nabla^2 \mu^-, \quad (9)$$

$$\nabla \cdot \mathbf{u}^- = 0, \quad (10)$$

$$\frac{\partial \mathbf{u}^-}{\partial t^-} = -\mathbf{u}^- \cdot \nabla \mathbf{u}^- - \nabla p^- + \frac{1}{Re_\tau} \nabla^2 \mathbf{u}^- + \frac{3}{\sqrt{8}} \frac{1}{We \cdot Ch} \mu^- \nabla \phi^-, \quad (11)$$

$$\mu = \phi^{3^-} - \phi^- - Ch^2 \nabla^2 \phi^-. \quad (12)$$

where Eq. (12) is the dimensionless chemical potential (2). The following dimensionless groups appear:

$$Re_\tau = \frac{U_\tau h}{\nu}, \quad Pe = \frac{U_\tau h}{M\beta}, \quad We = \frac{\rho U_\tau^2 h}{\sigma}, \quad Ch = \frac{\xi}{h}. \quad (13)$$

The shear Reynolds number ( $Re_\tau$ ) is the ratio between inertial forces and viscous forces, the Peclet number ( $Pe$ ) represents the interface relaxation time, the Weber number ( $We$ ) is the ratio between inertial forces and the surface tension and the Cahn number ( $Ch$ ) is the dimensionless capillary width. In our approach,  $Re_\tau$ ,  $Pe$ ,  $We$  and  $Ch$  are governing parameters that defined by considering the physical fluid properties, the flow regime, the simulated surface tension and the phase field modeling. Once the shear Reynolds number is fixed, the value of the surface tension is chosen by changing the Weber number. When considering immiscible fluids, the interface thickness depends on the numerical algorithm only, thus the Cahn number can be fixed to the smallest possible value. To obtain results independent from  $Ch$ , the Peclet number should be properly chosen: for this reason the scaling proposed by Magaletti et al. [15] has been adopted:  $Pe \propto Ch^{-1}$ . Eqs. (9)–(12) have been solved using a pseudo-spectral approach where periodicity conditions have been applied along the homogeneous directions  $x$  and  $y$  for both velocity field and order parameter; no-slip velocity and normal contact angle for the interface have been imposed at the walls [12,6]. The detailed numerical procedure can be found in [18].

**Table 1**

Collection of simulation parameters.

Simulation	$We$	$Re_\tau$	$Ch$	$Pe$	$\phi$
WE1	0.18	150	0.0185	168.2	0.053
WE2	0.21	150	0.0185	168.2	0.053
WE3	0.25	150	0.0185	168.2	0.053
WE4	0.28	150	0.0185	168.2	0.053
WE5	0.35	150	0.0185	168.2	0.053
WE6	0.71	150	0.0185	168.2	0.053
WE7	1.41	150	0.0185	168.2	0.053
WE8	2.83	150	0.0185	168.2	0.053

### 3.2. simulation parameters

In this work the shear Reynolds number based on the half channel height is  $Re_\tau = 150$ , leading to a fully developed turbulent flow. A large number of droplets of initial diameter  $d^- = 0.6$  yielding a volume fraction  $\phi = 0.053$  have been simulated considering wide range of Weber numbers:  $We = 0.18 \div 2.8$ . The droplet diameter is much larger than the Kolmogorov length scale  $\eta_{\bar{\kappa}}$  at all the positions in the domain: the ratio between the Kolmogorov length scale and the droplet diameter is  $0.027 \leq \eta_{\bar{\kappa}}/d^- \leq 0.063$ . The droplets diameter can increase due to coalescence; this effect has not been analysed, since this work focuses on the macroscopic droplets deformability. The simulations were run on a  $512 \times 256 \times 257$  fixed cartesian grid fine enough to resolve the smallest length scale of the turbulent flow, while the time step  $\Delta t^- = 10^{-4}$  has been chosen to resolve the smallest temporal scales and respond to the numerical stability requirements associated with the grid resolution. The pseudo-spectral scheme adopted can resolve accurately the interfacial layer with a minimum number of three mesh-points [6,7,18]. The interface is described by three mesh-points along  $x$  and  $y$  directions (where a uniform discretization is adopted) and by a minimum number of seven mesh-points along the  $z$  direction where a finer non-uniform discretization is adopted (Chebyshev polynomials). With reference to Eq. (5) the interface thickness (a layer where  $-0.9 \leq \phi^- \leq 0.9$ ) is fixed choosing  $Ch = 0.0185$  and, adopting the scaling law proposed by Magaletti et al. [15], the Peclet number is  $Pe = 162.2$ . The PFM cannot completely fulfill local mass conservation [19]; thanks to the accuracy of the numerical method and to the small interface thickness adopted, however, the mass loss is in any case small.<sup>2</sup> A collection of the relevant parameters of each simulation is reported in Table 1.

## 4. Results and discussion

Wall-drag modifications produced by large deformable droplets in a turbulent channel flow have been studied focusing the analysis on the correlation between the droplets deformability and the wall-drag modifications. Time-independent statistical results have been obtained by time and ensemble averaging (denoted by brackets “ $\langle \rangle$ ”); the time window adopted corresponds to  $\sim 24$  eddy turnover times  $T_e = h/U_\tau$ . All the results reported in this section are measured in wall-units “+” obtained by normalizing with  $U_\tau$ ,  $\rho$ ,  $\nu$  and  $\phi_+$ .

### 4.1. Qualitative analysis

Fig. 2a and b show the detail of one droplet moving in the near wall region for a small Weber number case (WE1) and a large Weber number case (WE6), respectively. The streamwise component of the velocity field relative to the droplet velocity ( $\mathbf{u}_d^+ = \mathbf{u}^+ - \mathbf{u}_d^+$ ) is shown by the contour plot reported on a  $x - z$

<sup>2</sup> After the entire simulation ( $2 \cdot 10^5$  time-steps, corresponding to  $\sim 50$  channel length covered by the mean flow), losses of volume  $V^-$  (or equivalently of mass  $m$ ) range from 2% to 10%.

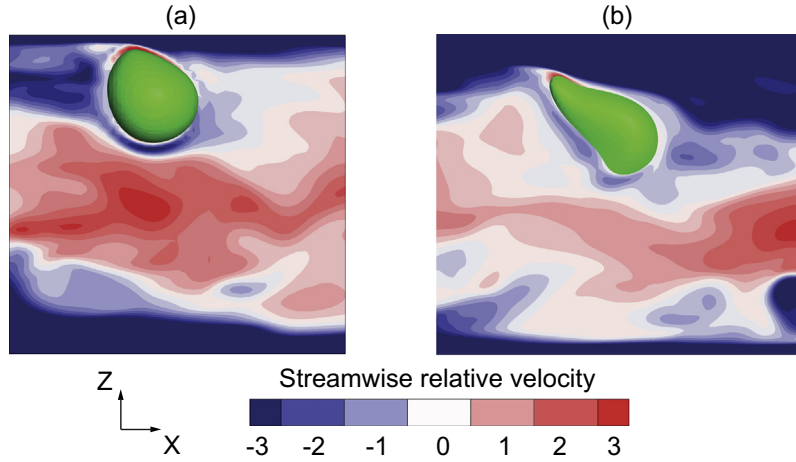


**Fig. 2.** Detail of the near-wall motion of a droplet for different Weber numbers: (a) simulation WE1, (b) simulation WE6. The contour plot of the streamwise velocity  $u_r^+$  relative to the droplet streamwise velocity  $u_d^+$  is depicted on a  $x-z$  plane passing across the droplet. The droplet interface is located by the iso-surface  $\phi = 0$  and is rendered in green. The entire computational domain along the wall-normal direction  $z$  is shown, while only a portion of  $\sim 300$  w.u. is shown along the streamwise direction.

slice that spans all the channel height (300 w.u.). The droplets are modified by the turbulent structures encountered in their motion: when the Weber number is small ( $We = 0.18$ ), the small deformations observed are limited to the near wall region and are probably due to the wall mean shear; when the Weber number is large ( $We = 0.71$ ), the deformations are much larger and the droplet assumes an elongated shape that is oriented in the direction of the stream flow. The relative velocity  $u_r^+$  increases reducing  $We$ : higher magnitude are measured in the channel center, while the regions of negative  $u_r^+$  shrink toward the walls. This effect is due to the droplet velocity  $u_d^+$  that decreases with  $We$ : in this particular case the less deformable droplet (WE1) has a mean velocity  $u_d^+ = 13.5$ , while the more deformable droplet (WE6) has a higher mean velocity  $u_d^+ = 16.7$ . Droplets with small deformability are slowed down by the near wall velocity field where they move in a negative relative velocity region, as observed in the fluid regions near the droplet of (Fig. 2a). The shape of droplets with large deformability show deformations that correlate with the relative velocity field: the droplet seems to be forced and deformed by two opposite sign flow regions (Fig. 2b): a region of positive  $u_r^+$  acting on its back side and a region of negative  $u_r^+$  insisting on its front side. As a result the flow field modifications are larger the smaller is the Weber number and droplets with large deformability can be more easily deformed by the surrounding flow field.

#### 4.2. Turbulence statistics

To analyze the effects of the droplets dispersed in the turbulent channel flow, first the streamwise mean velocity ( $u^+$ ) is measured.

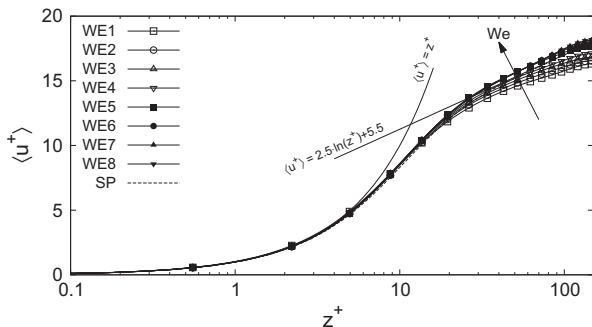


**Fig. 3.** Mean streamwise velocity profile ( $u^+$ ) along the wall-normal direction  $z^+$  for different Weber numbers. Arrow points in the increasing Weber number direction (increasing deformability).

Since the simulations are run with fixed average pressure gradient, the flow rate depends on the shear stress at the wall; small mean velocity fluctuations are ruled out by the ensemble and time averaging procedure. Fig. 3 shows that the mean streamwise velocity profile is shifted down when decreasing the Weber number (and thus the droplets deformability). Compared with the turbulence wall law, ( $u^+$ ) is reduced when  $We$  is small (WE1–WE4) and the resulting velocity profile is characterized by a logarithmic region that is shifted down and reduced in slope. In agreement with the observations of Lu et al. [4], droplets with small deformability produce Drag Enhancement (DE). On the contrary, when the  $We$  is large (simulations WE5–WE8), ( $u^+$ ) is slightly increased with respect to the single phase flow, but no significant Drag Reduction (DR) is observed. In order to correlate DE and DR with  $We$  and with the droplet deformability, the averaged friction coefficient  $C_f$  has been computed:

$$C_f = \frac{\tau_w}{\frac{1}{2}\rho\langle u_0 \rangle^2}, \quad (14)$$

where  $\langle u_0 \rangle$  is the flow average bulk velocity. Fig. 4a shows the friction coefficient normalized with its value measured for a single phase flow  $C_{f,s}$ ; plain dots refer to simulations where DE is observed, while filled dots are cases of no DE (or slight DR). The friction coefficient increases up to 11% for the smaller Weber number (simulation WE1), while a slight reductions of 1–2% is observed for large Weber numbers (simulations WE6–WE8). The DE observed in [4] for small Weber number bubbles was addressed to the flow obstruction produced by droplets with streamwise velocity smaller than the surrounding fluid. Based on this evidence the average droplets velocity  $u_d^+$  has been investigated. Fig. 4b shows that increasing the Weber number, the droplet average velocity increases reaching an almost uniform value when the DE vanishes (filled dots); this result confirms the qualitative behavior observed in Fig. 2 and it is in agreement with [4]. In particular, the droplet average velocity seems to correlate well with the inverse of the friction factor represented by the dashed line in Fig. 4b, confirming that the DE observed for small Weber number droplets is likely due to the slip velocity between the droplets and the surrounding fluid. While the DE mechanism and its dependence on  $We$  is recovered, the DR effect is in fact negligible in this simulations. In a flow where large and highly deformable bubbles are dispersed, the DR is mainly due to the streamwise vorticity canceling produced by the bubble motion in the near-wall region [4,5]. Fig. 5 shows the near-wall behavior of the Root Mean Square (RMS) of the streamwise vorticity fluctuations ( $RMS\langle \omega_x^+ \rangle$ ); when  $We$  is small (simulations WE1 and

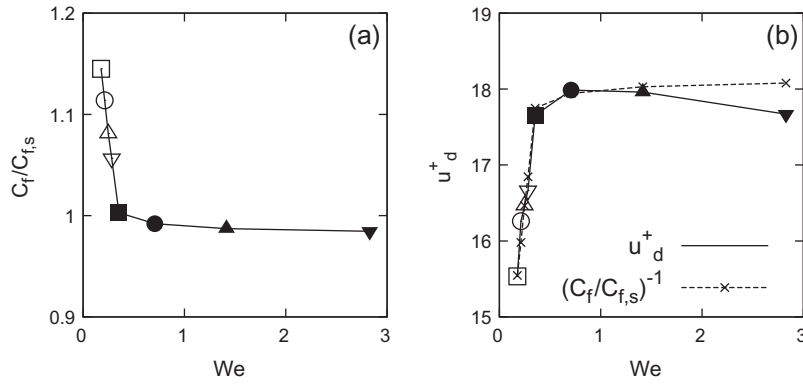


**Fig. 4.** Average friction coefficient  $C_f$  normalized with the single phase flow friction coefficient  $C_{f,s}$  for different Weber numbers (panel a). Droplets average velocity  $u_d^+$  for different Weber numbers (panel b). Plain dots refer to simulations where DE is observed; filled dots refer to simulations with no DE.

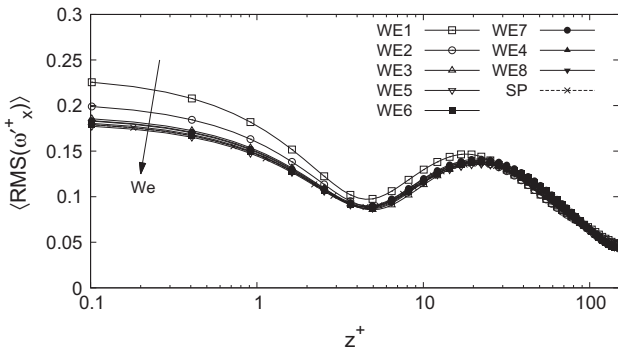


**Fig. 5.** Root Mean Square of the streamwise vorticity component fluctuations  $\langle \omega_x^+ \rangle$  along the wall-normal direction  $z^+$ . Arrow points in the increasing Weber number direction (increasing deformability).

WE2), the vorticity fluctuations at the wall are increased with respect to the single phase flow, while, when  $We$  is large (simulations WE5–WE8),  $\langle RMS(\omega_x^+) \rangle$  collapses over the single phase flow vorticity. Thus the presence of small  $We$  droplets is responsible for the enhancement of the near-wall streamwise vorticity fluctuations, while large  $We$  is not affecting  $\langle RMS(\omega_x^+) \rangle$ . In Fig. 6 the RMS of the spanwise vorticity fluctuations  $\langle RMS(\omega_y^+) \rangle$  is shown; in near-wall region there is an enhancement of  $\langle RMS(\omega_y^+) \rangle$  that is larger the smaller is  $We$  and the profiles collapse over the single phase flow curve when the  $We$  is large. In this region the wall-normal vorticity component (not displayed for brevity) has no major deviations from the single phase behavior. In the channel center (in a region from 70 w.u. to 230 w.u.) the spanwise vorticity fluctuations are increased reducing  $We$ ; this behavior is observed also in the

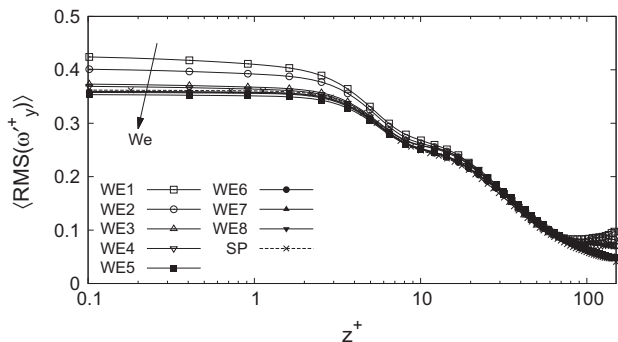


**Fig. 6.** Root Mean Square of the spanwise vorticity component fluctuations  $\langle \omega_y^+ \rangle$  along the wall-normal direction  $z^+$ . Arrow points in the increasing Weber number direction (increasing deformability).

wall-normal vorticity component (not displayed for brevity) which is affected in a similar way, but on a wider region (40–260 w.u.). The vorticity behavior suggests that when a droplet moves from the channel center towards the wall, it transports an higher streamwise velocity in the near wall region producing an increment of the near wall vorticity components. At the same time the droplet velocity is slowed down thus, when the droplet is transported again towards the center of the channel, it introduces a smaller streamwise velocity in that region. As a result the droplet is accelerated and the local vorticity fluctuations are enhanced. This mechanism is much more effective when the droplet behaves like a rigid body: once the velocity in some regions of the droplet surface are slowed down, also the neighborhood regions velocity are reduced because of the limited displacements allowed by the high surface tension. On the contrary when the droplet deformability is large, the interface can deform and adapt to the velocity difference in different regions, introducing a smaller obstruction to the flow (Fig. 2a).

### 5. Conclusions

The wall drag modification produced by large deformable bubbles or droplets dispersed in turbulent wall-bounded flows has large practical relevance but, due to the complexity of the analysis, only few detailed investigations are available. Recent results have shown that the droplets/bubbles deformability is central factor for the wall drag modification mechanism, thus, in this work, the wall drag modification produced by large droplets released in a turbulent channel flow is analyzed focusing on the role of the droplets deformability. The presence of the droplets produces an increment of the wall drag that decreases with the droplet deformability: significant DE is produced by the less deformable droplets, while these effects reduce increasing the deformability. When the deformability is sufficiently large, no DE is observed and an almost negligible DR is produced. The analysis of the droplet average velocity and of the vorticity fluctuations suggest that the DE is likely due to the droplet slip velocity. The absence of the vorticity canceling can be explained keeping into account the differences between the physical system considered here and the system considered by [4,5]: the inertia of the droplets considered in this work is much larger, thus the droplets can easily decorrelate from the vortical structures encountered. As a result the droplets do not produce the near-wall streamwise vorticity canceling and they act as a flow obstruction when their slip velocity increases.

### Acknowledgements

The authors acknowledge PRACE for awarding us access to resource JUROPA based in Germany at Julich. The authors

acknowledge the CINECA for the availability of high performance computing resources and support. The research was supported by the Italian Ministry for Research under the 2009 PRIN programme “Phase-field approach to chaotic mixing”.

## References

- [1] van den Berg TH, Luther S, Lathrop DP, Lohse D. Drag reduction in bubbly Taylor–Couette turbulence. *Phys Rev Lett* 2005;94:044501.
- [2] Sanders WC, Winkel EC, Dowling DR, Perlin M, Ceccio SL. Bubble friction drag reduction in a high-Reynolds-number flat-plate turbulent boundary layer. *J Fluid Mech* 2006;552:353–80.
- [3] Ceccio SL. Friction drag reduction of external flows with bubble and gas injection. *Ann Rev Fluid Mech* 2010;42:183–203.
- [4] Lu J, Fernandez A, Tryggvason G. The effect of bubbles on the wall drag in a turbulent channel flow. *Phys Fluids* 2005;17:095102.
- [5] van Gils DPM, Guzman DN, Sun C, Lohse D. The importance of bubble deformability for strong drag reduction in bubbly turbulent Taylor Couette flow. *J Fluid Mech* 2013;722:317–47.
- [6] Badalassi VE, Cenicerros HD, Banerjee S. Computation of multiphase systems with phase field model. *J Comput Phys* 2003;190:371–97.
- [7] Scarbolo L, Molin D, Perlekar P, Sbragaglia M, Soldati A, Toschi F. Unified framework for a side-by-side comparison of different multicomponent algorithms: Lattice Boltzmann vs phase field model. *J Comput Phys* 2013;234:263–79.
- [8] Cahn JW, Hilliard JE. Free energy of a nonuniform system I. *J Chem Phys* 1958;28:258–68.
- [9] Cahn JW, Hilliard JE. Free energy of a nonuniform system III. *J Chem Phys* 1959;31:688–700.
- [10] Sussman M, Smereka P, Hoshier S. A level set approach for computing solutions to incompressible two-phase flow. *J Comput Phys* 1994;114:146–59.
- [11] Jacqmin D. Calculation of two-phase Navier–Stokes flows using phase field modelling. *J Comput Phys* 1999;155:96–127.
- [12] Yue P, Feng JJ, Liu C, Shen J. A diffuse-interface method for simulating two-phase flows of complex fluids. *J Fluid Mech* 2004;515:293–317.
- [13] Anderson DM, McFadden GB. Diffuse-interface methods in fluid mechanics. *Ann Rev Fluid Mech* 1998;30:139–65.
- [14] Lamorgese AG, Molin D, Mauri R. Phase field approach to multiphase flow modelling. *Milan J Math* 2011;79:597–642.
- [15] Magaletti F, Picano F, Chinappi M, Marino L, Casciola CM. The sharp-interface limit of the Cahn Hilliard/Navier Stokes model for binary fluids. *J Fluid Mech* 2013;714:95–126.
- [16] Gurtin ME, Polignone D, Vinals J. Two-phase binary fluids and immiscible fluids described by an order parameter. *Math Models Meth Appl Sci* 1966;6:815.
- [17] Hohenberg PC, Halperin BI. Theory of dynamic critical phenomena. *Rev Mod Phys* 1977;49:435–79.
- [18] Scarbolo L, Soldati L. Turbulence modulation across the interface of a large deformable droplet. *J Turb* 2013;14:27–43.
- [19] Yue P, Zhou C, Feng JJ. Spontaneous shrinkage of drops and mass conservation in phase-field simulations. *J Comput Phys* 2007;223:1–9.